Schwank, M., Völksch, I., Wigneron, J.-P., Kerr, Y.H., Mialon, A., de Rosnay, P., Mätzler, C. (2010): Comparison of Two-Bare-Soil Reflectivity Models and Validation with L-Band Radiometer Measurements. - IEEE Transactions on Geoscience and Remote Sensing, 48, 1, 325-337

DOI: 10.1109/TGRS.2009.2026894

Comparison of Two Bare-Soil Reflectivity Models and Validation With L-Band Radiometer Measurements

Mike Schwank, Ingo Völksch, Jean-Pierre Wigneron, *Senior Member, IEEE*, Yann H. Kerr, *Senior Member, IEEE*, Arnaud Mialon, Patricia de Rosnay, and Christian Mätzler, *Senior Member, IEEE*

***Abstract*—The emission of bare soils at microwave L-band (1–2 GHz) frequencies is known to be correlated with surface soil moisture. Roughness plays an important role in determining soil emissivity although it is not clear which roughness length scales are most relevant. Small-scale (i.e., smaller than the resolution limit) inhomogeneities across the soil surface and with soil depth caused by both spatially varying soil properties and topographic features may affect soil emissivity. In this paper, roughness effects were investigated by comparing measured brightness temperatures of well-characterized bare soil surfaces with the results from two reflectivity models. The selected models are the air-to-soil transition model and Shi's parameterization of the integral equation model (IEM). The experimental data taken from the Surface Monitoring of the Soil Reservoir Experiment (SMOSREX) consist of surface profiles, soil permittivities and temperatures, and brightness temperatures at 1.4 GHz with horizontal and vertical polarizations. The types of correlation functions of the rough surfaces were investigated as required to evaluate Shi's parameterization of the IEM. The correlation functions were found to be clearly more exponential than Gaussian. Over the experimental period, the diurnal mean root mean square (rms) height decreased, while the correlation length and the type of correlation function did not change. Comparing the reflectivity models with respect to their sensitivities to the surface rms height and correlation length revealed distinct differences. Modeled reflectivities were tested against reflectivities derived from measured brightness, which showed that the two models perform differently depending on the polarization and the observation angle.**

***Index Terms*—Electromagnetic scattering by rough surfaces, microwave radiometry, permittivity, soil moisture.**

Manuscript received February 6, 2009; revised May 6, 2009 and June 25, 2009. First published September 9, 2009; current version published December 23, 2009. This work was supported in part by the Swiss Federal Institute for Forest, Snow and Landscape Research (Eidgenösische Forschungsanstalt für Wald, Schnee und Landschaft).

M. Schwank is with the Swiss Federal Institute for Forest, Snow and Landscape Research, CH-8903 Birmensdorf, Switzerland, and also with Gamma Remote Sensing Research and Consulting AG, CH-3073 Gümligen, Switzerland (e-mail: mike.schwank@wsl.ch).

I. Völksch is with the Swiss Federal Institute for Forest, Snow and Landscape Research, 8903 Birmensdorf, Switzerland (e-mail: ingo.voelksch@wsl.ch).

J.-P. Wigneron is with the Ecologie Fonctionnelle et Physique de l'Environnement, Institut National de Recherche Agronomiques, 33883 Bordeaux, France (e-mail: jpwigner@bordeaux.inra.fr).

Y. H. Kerr and A. Mialon are with the Centre d'Etudes Spatiales de la Biosphère, Centre National de la Recherche Scientifique/Centre National d'Etudes Spatiales/Institut de Recherche pour le Développement/Universite Paul Sabatier, 31401 Toulouse, France (e-mail: yann.kerr@cesbio.cnes.fr; mialon@cesbio.cnes.fr).

P. de Rosnay is with the Centre d'Etudes Spatiales de la Biosphère, Centre National de la Recherche Scientifique/Centre National d'Etudes Spatiales/Institut de Recherche pour le Développement/Universite Paul Sabatier, 31401 Toulouse, France, and also with the European Centre for Medium-Range Weather Forecasts, RG29AX Reading, U.K. (e-mail: Patricia.Rosnay@ecmwf.int).

C. Mätzler is with the Institute of Applied Physics, University of Bern, 3012 Bern, Switzerland (e-mail: christian.matzler@iap.unibe.ch).

Digital Object Identifier 10.1109/TGRS.2009.2026894

I. Introduction

ENERGY fluxes through the terrestrial surface layers are major drivers of climate. For land areas with sparse or no vegetation, the amount of this energy exchange is fundamentally linked with the moisture in the soil. Techniques for monitoring the surface moisture on the spatial scales relevant for climate and meteorological research are therefore of particular interest [1]–[5]. One such technique is passive microwave remote sensing at L-band (1–2 GHz), which has an almost 25-year-long history [6], [7]. It is used in the European Space Agency's (ESA) Soil Moisture and Ocean Salinity (SMOS) mission, which deduces soil surface moisture from thermal brightness at 1.4 GHz with near-global coverage every three days and a spatial resolution of approximately 40×40 km^2 [8], [9]. NASA's Soil Moisture Active and Passive (SMAP) mission will use a combined radiometer and high-resolution radar to measure surface soil moisture and freeze–thaw state. The mission is recommended by the U.S. National Research Council Committee on Earth Science and Applications from Space for launch between 2010 and 2013 [10].

Retrieving soil moisture from thermal microwave radiation is significantly affected by soil roughness [11]–[16]. Hence, the surface emission model used for interpreting measured radiance is one of the essential components in a retrieval algorithm. References [17]–[20] give an exhaustive review of the commonly used surface emission models relevant for passive microwave remote sensing. Most of the physical models, however, require significant computing effort and detailed ground truth information, which hampers their operative usage in retrieving algorithms. For this reason, easy-to-use semiempirical approaches such as the Q/H model [21], [22] are usually employed in retrieval algorithms.

This paper aims to test the application of two surface reflectivity models for retrieving the surface moisture of bare soils from measured L-band radiation. The two approaches studied are the so-called air-to-soil (A2S) transition model [12], [23, Ch. 4.7] and the physical integral equation model (IEM) [17]. With regard to the application in a retrieval algorithm, the

IEM model is evaluated using Shi's parameterization of a large database of IEM simulations. The A2S model describes the effect of soil roughness by matching the impedance between the dielectric constants of air and the topsoil. The gradual dielectric transition from air to soil is represented using a semiempirical effective medium approach. As demonstrated in [24]–[26], a similar approach can also be used for modeling the reflectivity of soils covered with sparse vegetation or litter, provided that scattering is not dominant.

The A2S and IEM models are compared in this study, and the model results are tested against the L-band signatures measured. The steps involved in the comparison are explained in Section II, and the experimental data set is presented in Section III. Results and discussion are the contents of Section IV, and conclusions are provided in Section V.

II. Models and Methods

A. Review of Existing Surface Reflectivity Models

The emissivity of a bare soil surface at horizontal ($p = \mathrm{H}$) or vertical polarization ($p = \mathrm{V}$) is described as $1 - R^p_{\mathrm{RM}}$, where R^p_{RM} is the surface reflectivity determining the brightness temperature T^p_{B} measured with an measured with the radiometer (RM). Two categories of surface reflectivity model can be distinguished: 1) physical approaches that seek solutions to Maxwell's equations by considering the boundary conditions on the rough surface and 2) empirical approaches that rely exclusively on observations.

The fast model developed by Shi *et al.* [27] can be considered physical, as it is a representation of reflectivities computed with the physical IEM [17]. The A2S transition model [12], [23, Ch. 4.7] can be classified somewhere in between the physical and the empirical approaches. The physical aspect of the A2S model is the concept of a vertically extended dielectric transition zone to model the gradual increase from the air to the bulk soil permittivity (impedance matching). The more empirical part of the A2S model is the representation of this dielectric transition zone by considering exclusively topographic features smaller than the resolution limit in combination with an empirical dielectric (refractive) mixing model.

According to [27], soil moisture can be retrieved with an accuracy of ≈3% if Shi's fast model is used. An analysis of horizontally polarized L-band signatures by means of the Shi reflectivity model and the A2S transition model is described in [12]. Mean deviations between the modeled and measured soil reflectivities were found to be 0.079 if the Shi model is applied and 0.029 if the A2S transition model is applied.

1) Shi's Parameterization of the IEM Model: Shi's fast model is used for the efficient computation of surface reflectivities predicted by the IEM. The fast model uses simulated reflectivity data derived from an advanced version of the IEM [28]. The IEM-simulated database consists of rough surface reflectivities for 1.4 GHz with horizontal ($p = \mathrm{H}$) and vertical ($p = \mathrm{V}$) polarizations and of reflectivities computed for exponential ($S = \mathrm{E}$) and Gaussian ($S = \mathrm{G}$) autocorrelation functions $C_S(r)$ of the rough surfaces. Additional input parameters to Shi's fast model are the surface root mean square (rms) height h, the correlation length lc, the surface permittivity ε_{s}, and the observation angle α relative to the vertical. The ranges of the IEM model parameters included in Shi's parameterization are $2.5\ \mathrm{mm} \leq h \leq 35\ \mathrm{mm}$, $25\ \mathrm{mm} \leq lc \leq 300\ \mathrm{mm}$, $20^\circ \leq \alpha \leq 60^\circ$, and $3.3 \leq \varepsilon_{\mathrm{s}} \leq 28.9$ (corresponding to the soil moisture range $0.02\ \mathrm{m^3 m^{-3}} \leq \theta \leq 0.44\ \mathrm{m^3 m^{-3}}$ if the empirical relation [29] is used).

Shi's fast model uses a parameterization of IEM-simulated reflectivities R^p_{IEM} consisting of a coherent ($R^p_{\mathrm{coh.}}$) and a noncoherent term ($R^p_{\mathrm{non\text{-}coh.}}$) [27]

$$R^p_{\mathrm{IEM}} = R^p_{\mathrm{coh.}} + R^p_{\mathrm{non\text{-}coh.}} = R^p_{\mathrm{F}} \cdot \exp\left[-\left(\frac{4\pi}{\lambda} h \cos\alpha\right)\right] + A^p \cdot R_{\mathrm{F}}^{pB^p}. \quad (1)$$

R^p_{F} is the Fresnel (F) reflectivity, λ is the wavelength (≈0.21 m), and A^p and B^p are the parameters given in [27] that depend on p, α, h, lc, and on the type of correlation function. As can be seen from (1), the coherent part $R^p_{\mathrm{coh.}}$ does not depend on the correlation length lc while the noncoherent part $R^p_{\mathrm{non\text{-}coh.}}$ depends on h and lc.

The hexagons shown in the flowchart in Fig. 1 show the inputs h, S, lc, ε_{s}, α, and p to be specified in Shi's parameterization and how they relate to the A2S model described next.

2) A2S Model: The uppermost soil horizon exhibits a highly complex 3-D structure in terms of the dielectric properties with feature sizes in the range of centimeters. These dielectric heterogeneities result not only from the surface roughness but also from spatial variations in moisture, texture, and structure.

The evaluation procedure and the basic ideas implemented in the A2S transition model are shown in the diagrams in Figs. 1 and 2. The model takes into account how many of the soil topographic features are smaller than the resolution limit at L-band frequencies, which can be estimated by the Bragg limit Λ_{Bragg}(λ = wavelength, α = observation angle)

$$\Lambda_{\mathrm{Bragg}} = \frac{\lambda}{2\sin\alpha}. \quad (2)$$

The Bragg limit Λ_{Bragg}, however, is not a sharp criterion to distinguish between the small features to be treated in the sense of full-wave electromagnetism and the larger features that can be modeled with geometric optics. The resolution limit Λ_{Bragg} gives the order of magnitude of the spatial dimension in which the intermediate method of physical optics applies. From now on, the expression "small scale" (SS) is used for feature sizes with dimensions smaller than the resolution limit.

Dielectric SS heterogeneities [cross section shown in Fig. 2(a)] can therefore be treated in the sense of the quasi-static limit, where the mean field is homogeneous and extends over a region much larger than the feature size. This makes it possible to postulate an A2S transition zone [Fig. 2(b)] matching the impedance between the air and bulk soil. Within this zone, the effective permittivity $\varepsilon(z)$ [30] gradually increases from the air value ($\varepsilon_{\mathrm{a}} = 1$) to the permittivity $\varepsilon_{\mathrm{s}} > \varepsilon_{\mathrm{a}}$ of the bulk surface soil.

The apparent dielectric profile $\varepsilon(z)$ shown in Fig. 2(d) is modeled with the refractive mixing model [30], [31], taking into account the bulk soil and air phases

$$\varepsilon(z) = \left[\nu(z)\varepsilon_{\mathrm{s}}^{1/2} + [1 - \nu(z)]\,\varepsilon_{\mathrm{a}}^{1/2}\right]^2. \quad (3)$$

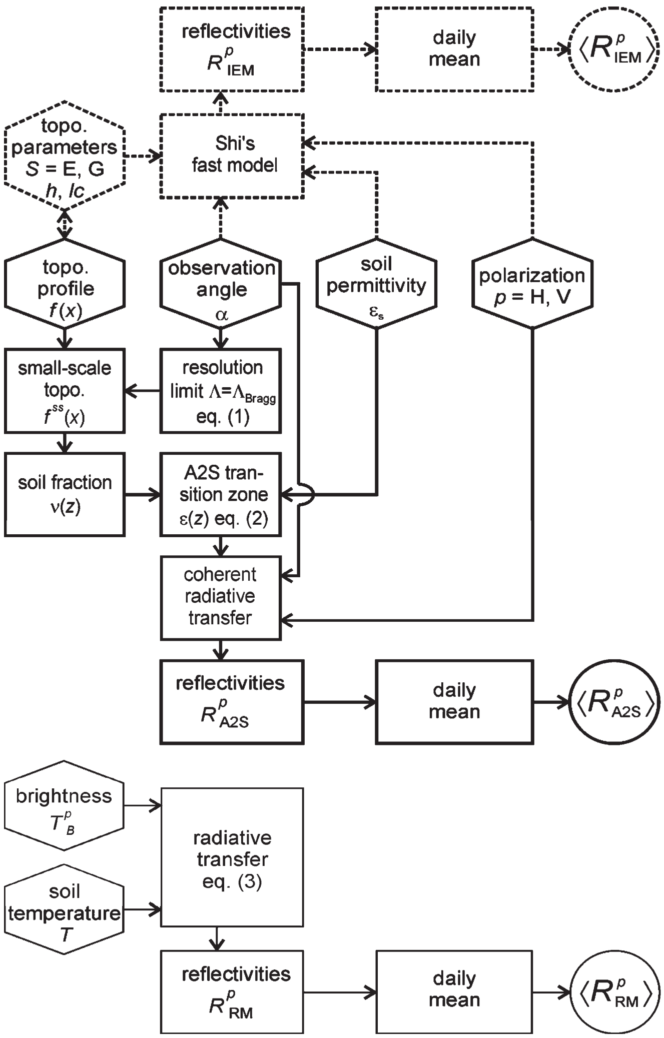

Fig. 1. Illustration of the procedures applied for deriving rough surface reflectivities $R^p_M (p = \text{H}, \text{V}; M = \text{IEM, A2S, RM})$. Hexagons indicate model inputs. (Dashed-line boxes) Reflectivities R^p_{IEM} computed with the IEM model require the topography parameters h, lc, $S = \text{E}, \text{G}$ [either preset or derived from topography profiles $f(x)$]. (Solid-line boxes) Reflectivities R^p_{A2S} computed with the A2S model directly use $f(x)$ as input. (Thin-line boxes) Reflectivities R^p_{RM} are derived from measured brightness and soil temperatures T^p_{B} and T.

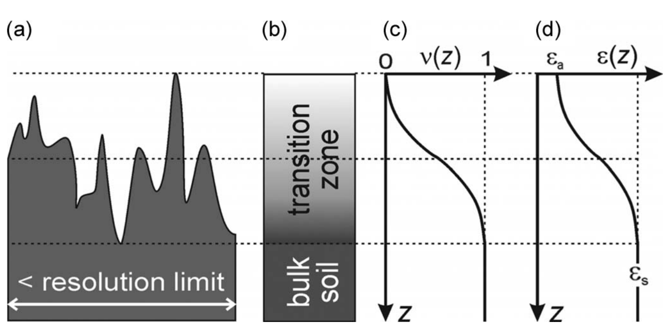

Fig. 2. Illustration of the ideas implemented in the A2S transition model. A cross section of the small scale (SS) topography is shown as a sketch in (a). The postulated A2S transition zone is shown in (b). The volumetric soil fraction $\nu(z)$ and the dielectric profile $\varepsilon(z)$ computed with (3) are shown in (c) and (d), respectively.

Thereby, the volume fraction $\nu(z)$ of the bulk soil phase [Fig. 2(c)] increases with depth z, whereas the air fraction $1 - \nu(z)$ decreases to zero within the A2S transition zone. In [23, Ch. 4.7], where the A2S model is explained in detail, $\nu(z)$ is represented by an empirical relation comprising its vertical extent. For our study, either measured or synthetically generated topography data are available, allowing $\nu(z)$ to be modeled as the cumulated probability density of the SS surface height (see Section II-C).

Imaginary parts of bulk soil permittivities ε_{s} used in (3) were not considered as only real parts were available from the capacitive *in situ* measurements (see Section III). Finally, once the dielectric depth profile $\varepsilon(z)$ is modeled from the SS topography, the rough soil reflectivities R^p_{A2S} $(p = \text{H}, \text{V})$ are calculated by applying a coherent radiative-transfer model for layered dielectric media. A matrix formulation of the boundary conditions at the layer interfaces derived from Maxwell's equations is used [32]. This coherent model was evaluated for dielectric layers with thickness $d = 0.1$ mm $\ll \lambda$, making the reflectivities R^p_{A2S} independent of d.

B. Microwave Radiative Transfer

L-band brightness temperatures T^p_{B} with horizontal $(p = \text{H})$ and vertical $(p = \text{V})$ polarizations measured with the RM are used for deriving soil reflectivities R^p_{RM} (thin-line boxes in Fig. 1). This requires a radiative transfer model expressing T^p_{B} by means of R^p_{RM}, the effective physical temperature T [33] of the soil surface layer, and the mean sky brightness temperature $T_{\text{B,sky}} \approx 6.3$ K [34]

$$T^p_{\text{B}} = T\,(1 - R^p_{\text{RM}}) + T_{\text{B,sky}} R^p_{\text{RM}}. \tag{4}$$

Equation (4) fulfills Kirchhoff's law and can easily be solved for R^p_{RM}. Validations of the reflectivity models presented in Section IV-C are performed by means of daily mean values $\langle R^p_{\text{RM}} \rangle$ computed from instantaneous R^p_{RM}. This approach was chosen as reliable topography information, which is required as input to the reflectivity models, was available on a daily basis only.

C. Rough Surfaces

The purpose of Sections II-C1 to C5 is to describe the modeling steps shown in Fig. 1. Following this, reflectivities R^p_M $(p = \text{H}, \text{V}; M = \text{A2S}, \text{IEM})$ at the observation angles α are modeled from topography profiles $f(x)$ of random rough soil surfaces with permittivities ε_{s}. The surface topography $f(x)$ is either measured directly (see Section III) or artificially generated (see Section II-C1). To derive R^p_{A2S}, the SS topography $f^{\text{ss}}(x)$ is extracted from $f(x)$ (Section II-C2), and then, the soil fraction profile $\nu(z)$ is determined (Section II-C3), leading to the dielectric profile $\varepsilon(z)$ (3) used for computing R^p_{A2S}. The computation of the rms height h, the correlation function $C(r)$, and the correlation length lc of $f(x)$ required for computing R^p_{IEM} is described in Section II-C4. Section II-C5 introduces the quantity EG used for rating the type of measured correlation function to be specified in Shi's fast model.

1) Generating Surface Topographies: As the flowchart in Fig. 1 shows with the solid-line boxes, modeling R^p_{A2S} requires the topography data of a rough dielectric surface. For this purpose, 1-D random rough surface profiles $f_S(x)$ with either Gaussian ($S = \mathrm{G}$) or exponential ($S = \mathrm{E}$) correlation functions $C_S(r)$ are generated

$$C_{\mathrm{G}}(r) = \exp\left(-\frac{r^2}{lc^2}\right) \text{ and } C_{\mathrm{E}}(r) = \exp\left(-\frac{|r|}{lc}\right). \quad (5)$$

Thereby, r denotes the horizontal distance in x between two points of the surface, and the $C_S(r)$ evaluated at r expresses the statistical correlation between the surface heights $f_S(x)$ and $f_S(x+r)$. From $C_{\mathrm{G}}(lc) = C_{\mathrm{E}}(lc) = e^{-1} \approx 0.37$, it follows that the correlation between two surface heights at the characteristic distance $r = lc$ is the same for the exponential and the Gaussian surface type.

For generating exponential and Gaussian profiles $f_S(x)$ of length L, zero mean $\langle f_S(x)\rangle = 0$, rms heights h, and correlation lengths lc, the approach described in [35, Ch. 4] was implemented. The power spectral densities [19, Ch. 4 and Sec. 1.4]

$$W_{\mathrm{G}}(k) = \frac{h^2 lc}{2\sqrt{\pi}} \exp\left(-\frac{k^2 \cdot lc^2}{4}\right) \quad W_{\mathrm{E}}(k) = \frac{h^2 \cdot lc}{\pi(1+k^2 lc^2)} \quad (6)$$

associated with the two surface types express the abundance of features with a certain spatial wavenumber $k = 2\pi/\Lambda$ present in $f_S(x)$ (Λ = spatial wavelength). As a consequence of the exponential form of $W_{\mathrm{G}}(k)$ associated with the Gaussian surface $f_{\mathrm{G}}(x)$, the spectral components with $k \geq k_{lc} \equiv 2\pi/lc$ (corresponding to $\Lambda \leq lc$) are clearly less present in a Gaussian than in an exponential surface generated for the same lc and h. Quantitatively, this can be expressed by the fraction EG_S, weighing the spectral components with spatial wavelengths Λ shorter than lc

$$EG_S \equiv \frac{\int_{k_{\mathrm{lc}}}^{\infty} W_S(k)dk}{\int_0^{\infty} W_S(k)dk} = \begin{cases} 1-\mathrm{Erf}\pi \approx 10^{-5}, & \text{for } S=\mathrm{G} \\ 2/\pi \mathrm{ArcCot} 2\pi \approx 10^{-1}, & \text{for } S=\mathrm{E}. \end{cases} \quad (7)$$

The distinct difference between EG_{G} and EG_{E} suggests that this quantity can be applied to measured topography data to decide whether the surface is exponential or Gaussian. This will be pursued in Section II-C5 and applied in Section IV-A to investigate whether the type of correlation function changes with time as a consequence of the progressive weathering of the soil surface.

2) Filtering of Small Scale (SS) Features: The A2S transition model uses exclusively SS surface features $f^{\mathrm{ss}}(x)$ with spatial dimensions smaller than the resolution limit (Figs. 1 and 2) to compute R^p_{A2S}. As mentioned in Section II-A2, the Bragg resolution limit Λ_{Bragg} is not an exact lower limit for the dimension of features that can be electromagnetically resolved. Considering this, it has to be emphasized that defining small scale (SS) as features with dimensions smaller than Λ_{Bragg} means there is a certain model uncertainty.

However, a discrete Fourier high-pass filter with the Bragg resolution limit (2) chosen for the cutoff wavelength is applied to extract the SS features $f^{\mathrm{ss}}(x)$ with $\Lambda \leq \Lambda_{\mathrm{Bragg}}$ from $f(x)$. Applying discrete Fourier transformations to a profile of length L requires first transforming the data into an equidistant form $[x_j, z_j]$ $(j=1,\ldots,N)$ with increments $\Delta x = L/(N-1)$ along the horizontal direction x. Subsequently, the data $[L+j\cdot\Delta x, z_{N-j}]$ $(j=1,\ldots,N-1)$ are appended to $[x_j, z_j]$, resulting in a periodic sequence $2L$ in length and $N_0 = 2N-1$ data points. This complemented periodic data set can now be represented by its Fourier series

$$z_j = \sum_{k=0}^{N_0-1} c_k \exp\left(2\pi i \frac{k(j-1)}{N_0}\right) \quad (8)$$

with the complex Fourier coefficients c_k given by

$$c_k = \frac{1}{N_0}\sum_{j=1}^{N_0} z_j \exp\left(-2\pi i \frac{k(j-1)}{N_0}\right). \quad (9)$$

Then, the SS features $[x_j, z_j^{\mathrm{ss}}]$ $(j = 1,\ldots,N)$ required to compute the soil fraction $\nu(z)$ are extracted by evaluating the Fourier series (8) with c_k computed from (9) for $\Lambda = 2L/k \leq \Lambda_{\mathrm{Bragg}}$, and, otherwise, with $c_k = 0$.

3) Soil Fraction in the A2S Transition Zone: The soil fraction $\nu(z)$ within the A2S transition zone (Fig. 2) is computed from the discrete SS topography data $[x_j, z_j^{\mathrm{ss}}]$ $(j = 1,\ldots,N)$ by using the "Quantile" function implemented in "Mathematica 5.2." Calling this function with the vector z_j^{ss} and a certain probability P between zero and one yields the height z at which the air fraction $1-\nu(z)$ equals P. Thus, the discrete data set $[z_j, \nu_j]$ considering $N-1$ evenly spaced soil fraction levels $0 < \nu_j < 1$ is constructed. The corresponding continuous interpolation function $0 < \nu(z) < 1$ is then used in the refractive dielectric mixing model (3) to describe the apparent dielectric profile $\varepsilon(z)$ used to compute the reflectivity R^p_{A2S} with the A2S model.

4) Correlation Function and Correlation Length: When topography profiles $f(x)$ are measured, they are characterized by their correlation length lc and rms heights h. For an equally spaced topography data set $[x_j, z_j]$ $(j = 1,\ldots,N)$, h is simply computed as the standard deviation of the heights z_i. To derive the lc of a profile with length L, the correlation function $C(r)$ has to be computed numerically

$$C(r) \equiv \frac{1}{Lh^2}\int_0^L [f(x)-\langle f\rangle][f(x+r)-\langle f\rangle]\, dx. \quad (10)$$

To enable the evaluation of (10) for each r in the range of $0 \leq r \leq L$ considering the given integration limits, the data $[x_j, z_j]$ must be supplemented with their mirrored sequence (compare Section II-C2). The resulting continuous correlation function $C(r)$ associated with $[x_j, z_j]$ is then used to compute the correlation length lc by solving $C(lc) = e^{-1}$ numerically for the smallest solution.

At this point, it should be noted that the length L of a profile may have a significant influence on the estimated h and lc. Monte Carlo simulations showed that the 95% confidence limits for the h and lc of individual transects come into $\pm 10\%$ margin of error when L is around $240 \cdot lc$ and $460 \cdot lc$ [36]. The same investigation showed that the mean values $\langle h \rangle$ and $\langle lc \rangle$ derived from a set of realizations are much more reliable. Considering these findings and in view of the fact that measured profiles were available for $L = 2$ m, it is expected that the h and lc derived from the individual profiles are rather error prone. Their daily mean values $\langle h \rangle$ and $\langle lc \rangle$ derived from the 11 to 16 profiles available per day, however, are expected to be much more representative of the surface state on a particular day.

5) Correlation Function Type: Reflectivities R^p_{IEM} computed with Shi's parameterization of IEM reflectivities are rather sensitive to the type of the correlation function of the topography. Therefore, indicator values EG that allow systematic trends in time in the surface correlation function type to be identified (Section IV) are calculated

$$EG \equiv \frac{\sum\limits_{k \geq 2\pi/lc} |c_k|^2}{\sum\limits_{k} |c_k|^2}. \tag{11}$$

In analogy with (7), EG weighs the sum of the squared absolute values of the Fourier coefficients c_k (9) with wavenumbers $k \geq 2\pi/lc$ (corresponding to spatial wavelengths $\Lambda \leq lc$) with respect to the total sum of $|c_k|^2$. Consequently, EG defined by (11) weighs the spectral components with spatial wavelengths Λ shorter than lc and can therefore be used to rate the type of correlation function measured as either more exponential or Gaussian.

III. SMOSREX Dataset

The two reflectivity models were validated with a long-term data set acquired in the framework of the Surface Monitoring of the Soil Reservoir Experiment (SMOSREX), which has been in full operation since January 2003 [37]. L-band brightness temperatures T^p_{B} $(p = \mathrm{H}, \mathrm{V})$ of a bare soil site are acquired by the L-band radiometer (RM) for Estimating Water In Soils (LEWIS), installed near Toulouse in the south of France [38]. The LEWIS RM is mounted at the top of a 13.7-m vertical structure and provides T^p_{B} with an accuracy of ± 0.2 K. The field of view of the horn antenna is 13.5° at -3 dB. Every 3 h, elevation scans at $\alpha = 20°, 30°, 40°, 50°,$ and $60°$ are performed over the bare soil and a plot with vegetation. The bare soil was rather smooth until January 13, 2006, which we refer to as DoY $= 13$, where DoY is the day of year. On that date, it was plowed, and the surface roughness was distinctly increased. Up until that date, the soil structure had not been modified artificially and had just changed gradually with climatic events (rainfall, wind, etc.).

After plowing, changes in the soil topography were monitored by regularly measuring the soil mechanically. For this purpose, a needle board that is 2 m in length L, consisting of $N = 201$ movable (in the vertical direction) needles that are 1 cm apart, is used to follow the soil elevation profile. Photos of the board are taken, manually digitized, and finally used to compute soil topography profiles $f = [x_j, z_j]$ $(j = 1, \ldots, N)$. Measurements were performed parallel and perpendicular to the soil rows produced through plowing. After plowing, 11 assessments were conducted in 2006, i.e., DoY $= 13, 20, 32, 51, 75, 93, 124, 150, 181,$ and 328, and one in 2007 (DoY $= 71$).

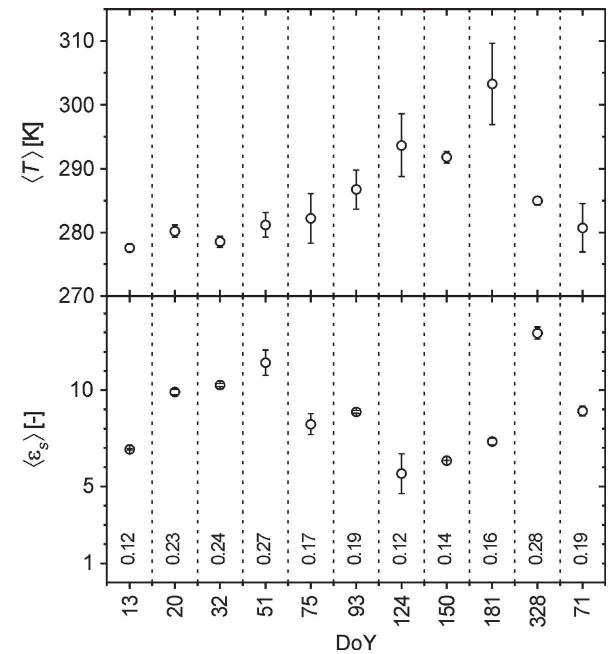

Fig. 3. Daily mean values and standard deviations of (top panel) soil temperature $\langle T \rangle \pm \sigma_T$ and (bottom panel) real parts of soil permittivity $\langle \varepsilon_{\mathrm{s}} \rangle \pm \sigma_\varepsilon$ measured within the top 6 cm of the soil. The numbers above the DoY axis indicate volumetric soil moistures θ (cubic meter per cubic meter).

In addition to these topography measurements, the real part ε_{s} of the soil permittivity and soil temperature profiles T were monitored every 30 min throughout the whole experiment with a set of capacitive probes (Theta Probe) and thermistors installed at different soil depths down to 90 cm. Daily mean values $\langle \varepsilon_{\mathrm{s}} \rangle \pm \sigma_\varepsilon$ and $\langle T \rangle \pm \sigma_T$ recorded with the probes installed within the topmost 6 cm of the soil are shown in Fig. 3. Estimates of the volumetric moisture θ (cubic meter per cubic meter) computed with the empirical model [29] are indicated above the DoY axis of the bottom panel. These data measured *in situ* will be used in Section IV-C in the comparison between modeled soil reflectivities and those deduced from measured L-band signatures T^p_{B}. The soil type near the surface was silt loam to loam according to the Food and Agriculture Organization/U.S. Department of Agriculture classification system, while at deeper soil layers, a richer clay content was found.

IV. Results and Discussion

A. Soil Topographies

Surfaces $f_{\mathrm{E}}(x)$ with exponential correlation functions are associated with nondifferentiable topographies. This is typical for granular media with loose crumbs and cracks at the surface. Gaussian surfaces $f_{\mathrm{G}}(x)$, by contrast, are differentiable and, thus, locally smooth, as is sometimes the case with the surface of a liquid. With regard to the soil topographies measured, it was hypothesized that the surfaces measured during the first days after plowing would be mostly exponential. The second hypothesis was that the surfaces would become more Gaussian after several rain events. These two hypotheses will be discussed in the following Sections IV-A1 and A2.

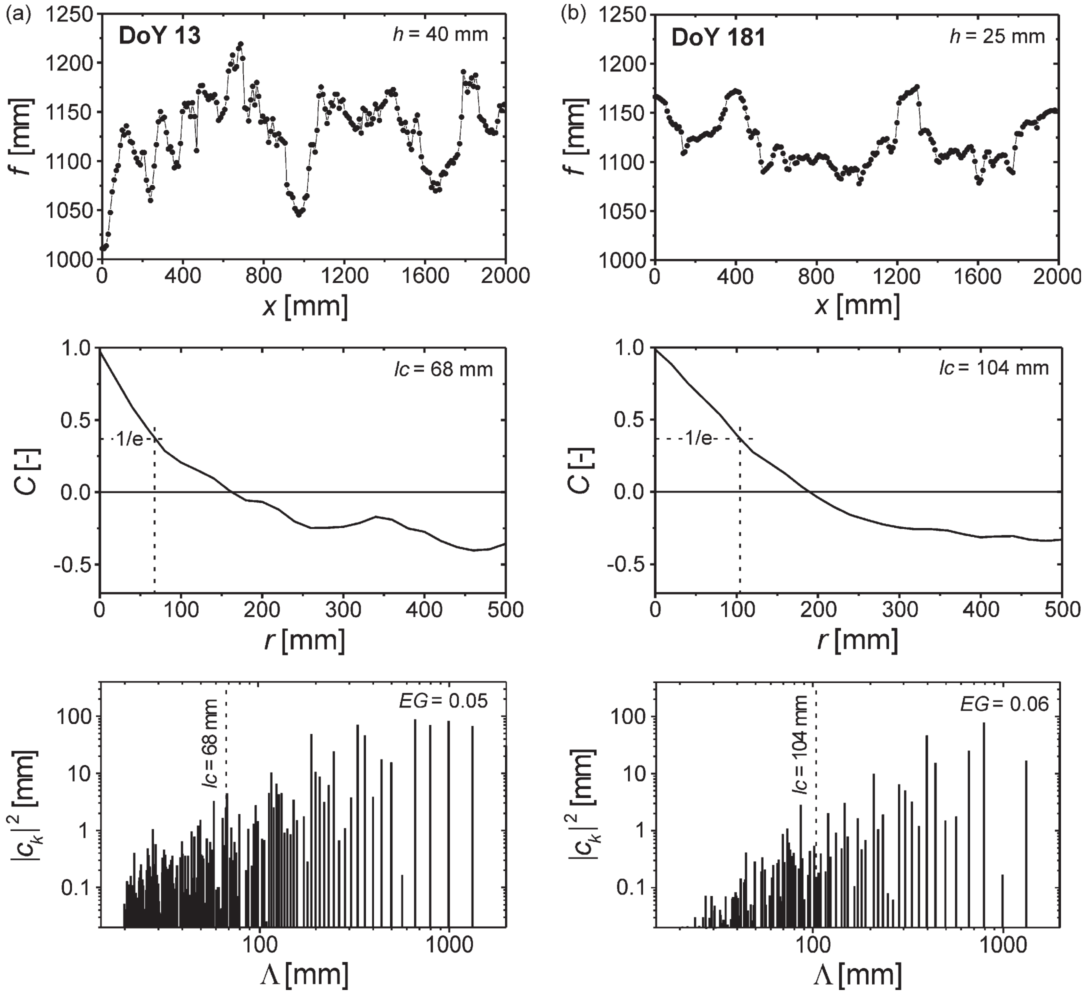

Fig. 4. Topography profiles f measured with the needle board ($N = 201$ measuring points and length $L = 2$ m) on (a) DoY 13 and on (b) DoY 181. Surface rms heights are $h = 40$ mm and $h = 25$ mm. The middle panels show (dashed lines) the associated correlation functions $C(r)$ with $lc = 68$ mm and $lc = 104$ mm. The power spectra of f [c_k = Fourier coefficients (9)] plotted versus the spatial wavelengths Λ are shown in the bottom panels with EG [defined in (11)] indicated.

1) Topography and How It Changes With Time: To illustrate how the topography of the soil changed after it was plowed until the end of the experiment, an early topography profile and one of the last profiles taken from the SMOSREX data set (Section III) were analyzed. The rms height h and the correlation length lc derived from the two single profiles are not necessarily representative of the surface state on the corresponding days. As discussed in Section II-C4, the surface statistical parameters h and lc could be disputed due to the limited profile length ($L = 2$ m).

The top panels of Fig. 4(a) and (b) show surface profiles f for January 13, 2006 (DoY 13 = day of plowing) and June 30, 2006 (DoY 181). The middle panels show the corresponding correlation functions $C(r)$, and the bottom panels show the surface power spectra $|c_k|^2$ (9) plotted versus the spatial wavelength $\Lambda = 2L/k$.

The topography of the freshly plowed field (DoY 13) clearly differs from that measured 5.5 months later on DoY 181. This change is conveyed by the rms height decreasing from $h = 40$ mm (DoY 13) to $h = 25$ mm (DoY 181) and the correlation length increasing from $lc = 68$ mm (DoY 13) to $lc = 104$ mm (DoY 181). The values $EG \approx 0.05$ for DoY 13 and $EG \approx 0.06$ for DoY 181 are similar and of the same order of magnitude as the $EG_{\mathrm{E}} \approx 10^{-1}$ for exponential surfaces. By contrast, Gaussian surfaces reveal significantly smaller $EG_{\mathrm{G}} \approx 10^{-5}$ (7). This implies that the two topography profiles measured comprise a rather large fraction of features smaller than lc, which suggests that the topographies are more likely to be exponential than Gaussian. However, just two surface profiles are not sufficient to determine this.

2) Daily Mean Soil Surface Properties: To test the results of Fig. 4 further, an extended database, consisting of profiles $f = [x_j, z_j]$ measured on DoY $= 13, 20, 32, 51, 75, 93, 124, 150, 181,$ and 328 in 2006 and DoY $= 71$ in 2007, was analyzed. In this database, 11–16 profiles are available for each of the 11 days. Daily mean values $\langle h \rangle \pm \sigma_h$, $\langle lc \rangle \pm \sigma_{lc}$, and $\langle EG \rangle \pm \sigma_{EG}$ with their corresponding standard deviations are shown in Fig. 5(a)–(c), respectively. The bold dots represent h, lc, and EG of the two single profiles in Fig. 4. As mentioned in Section II-C4, unlike h, lc, and EG, the daily mean values $\langle h \rangle$, $\langle lc \rangle$, and $\langle EG \rangle$ can be expected to be representative of the soil topography on the days considered.

As can be seen in Fig. 5(a), $\langle h \rangle$ gradually decreased from $\langle h \rangle = 39$ mm on the day of plowing (DoY 13, 2006) to

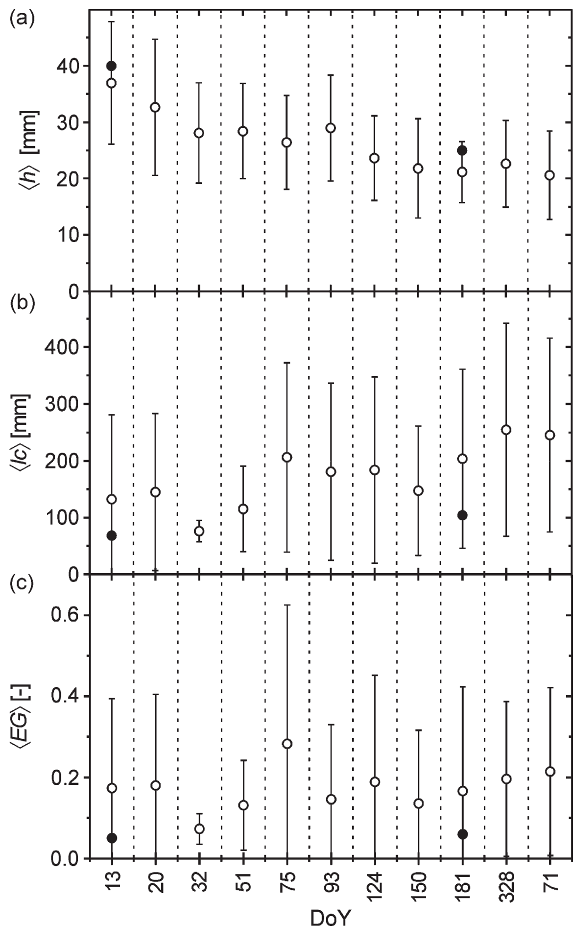

Fig. 5. (Open dots, ○) (a) Daily mean surface rms height $\langle h\rangle \pm \sigma_h$, (b) correlation length $\langle lc\rangle \pm \sigma_{lc}$, and (c) $\langle EG\rangle \pm \sigma_{EG}$ defined in (11) derived from topographies measured on the indicated days. The bold dots (●) on DoY 13 and DoY 181 are the h, lc, and EG of the profiles from Fig. 4.

approximately $\langle h\rangle = 20$ mm 14 months later (DoY 71, 2007). This confirms the hypothesis that soil roughness decreases with time due to progressive weathering and concretion caused by successive rain events. The standard deviations σ_h and σ_{lc} of the surface rms height h and the correlation length lc do not, however, decrease with time. This indicates that the wide variation in h on the meter scale tends to be rather persistent despite weathering processes. Furthermore, it corroborates the difficulty of assigning a distinct correlation length to a soil surface based on relatively short topography profiles. Considering the consistently large σ_{lc}, no clear temporal trend can be identified for $\langle lc\rangle$. This means that the increase of $lc = 68$ mm deduced from the profile on DoY 13 to $lc = 104$ mm for the profile on DoY 181 (Fig. 4) is not representative, and therefore, the hypothesis that the correlation length of the soil surface increases with time is not confirmed.

The daily values $\langle EG\rangle \pm \sigma_{EG}$ computed to infer the suspected temporal trend in the correlation function type from exponential $[EG_{\mathrm{E}} \approx 10^{-1}$ (7)] to more Gaussian $(EG_{\mathrm{G}} \approx 10^{-5})$ remained at the same level over the entire observation period. According to definition (11), this implies that the proportion of surface features with spatial wavelengths $\Lambda < lc$ does not change with time. However, the A2S model uses exclusively SS features with dimensions smaller than the resolution limit Λ_{Bragg} (2), which is important to bear in mind with regard to the temporal evolution of the daily mean reflectivities $\langle R^p_{\mathrm{A2S}}\rangle$.

Given the finding that $\langle EG\rangle$ does not reveal a clear trend over the 14 months after plowing the field, a mean value $\langle EG_{\mathrm{tot}}\rangle$ can be assigned. The overall mean $\langle EG_{\mathrm{tot}}\rangle = 0.17$ is in agreement with $EG_{\mathrm{E}} \approx 10^{-1}$ (7) associated with an ideal exponential surface $f_{\mathrm{E}}(x)$. This implies that Shi's fast model should be evaluated for the exponential surface type to generate IEM reflectivities potentially reproducing remotely sensed soil reflectivities.

B. Comparison of Modeled Rough Surface Reflectivities

In this section, we present the modeled reflectivities R^p_{IEM} and R^p_{A2S} $(p = \mathrm{H}, \mathrm{V})$ at 1.4 GHz of rough dielectric surfaces. Evaluations were performed for the soil permittivity $\varepsilon_{\mathrm{s}} = 10$ (corresponding to the soil moisture $\theta \approx 0.20$ m^{3}m^{-3} if the model [29] is used). The observation angles $\alpha = 35°$ and $55°$ were chosen to be consistent with the radiometer observations presented in Section IV-C.

To explore the model responses with respect to h and lc, the reflectivities shown in Figs. 6 and 7 were computed for the parameter ranges: 1) $R^p_{\mathrm{A2S}}(h)$ (open dots) and $R^p_{\mathrm{IEM}}(h)$ (solid dots) for $h \leq 100$ mm and constant $lc = 100$ mm and 2) $R^p_{\mathrm{A2S}}(lc)$ (open dots) and $R^p_{\mathrm{IEM}}(lc)$ (solid dots) for $lc \leq 490$ mm and constant $h = 20$ mm. The panels (a) show reflectivities for horizontal polarization $(p = \mathrm{H})$, and the panels (b) show reflectivities for vertical polarization $(p = \mathrm{V})$. Reflectivities R^p_{A2S} are derived from surface profiles $f(x) = [x_j, z_j]$ generated for the set points h and lc. As these profiles are random in nature, a Monte Carlo approach is used to compute the ranges $R^p_{\mathrm{A2S}} \pm \sigma^p_{R\ \mathrm{A2S}}$ representative of the h and lc considered. Each $R^p_{\mathrm{A2S}} \pm \sigma^p_{R\ \mathrm{A2S}}$ shown in Figs. 6 and 7 is computed from the particular reflectivities deduced from 100 profiles $f(x) = [x_j, z_j]$ $(j = 1, \ldots, N = 201)$ with length $L = 2$ m.

The gray shaded areas indicate the sensitivity of R^p_{A2S} with respect to the choice of the maximum spatial wavelength Λ used to extract the SS roughness with feature sizes smaller than the resolution limit. As discussed in Section II-C2, the cutoff $\Lambda = \Lambda_{\mathrm{Bragg}}$ is normally used to evaluate the A2S model, which implies that topography features with $\Lambda \leq \Lambda_{\mathrm{Bragg}}$ are exclusively considered. The upper boundaries of the gray areas in Figs. 6 and 7 are R^p_{A2S}, computed with $\Lambda = \Lambda_{\mathrm{Bragg}}/2$, and the lower boundaries are for $\Lambda = \Lambda_{\mathrm{Bragg}} \cdot 2$.

As can be seen in Fig. 6, the two reflectivity models give identical results for the specular case $(h \to 0$ mm). As expected, they also coincide with the Fresnel reflectivities, R^p_{F} computed for $\varepsilon_{\mathrm{s}} = 10$ and $\alpha = 35°$ and $55°$. For horizontal polarization, $R^{\mathrm{H}}_{\mathrm{IEM}}(h)$ and $R^{\mathrm{H}}_{\mathrm{A2S}}(h)$ are in agreement within the A2S model uncertainty associated with the choice of the cutoff wavelength $\Lambda_{\mathrm{Bragg}}/2 \leq \Lambda \leq \Lambda_{\mathrm{Bragg}} \cdot 2$ used. With vertical polarization, however, the differences between $R^{\mathrm{V}}_{\mathrm{IEM}}(h)$ and $R^{\mathrm{V}}_{\mathrm{A2S}}(h)$ cannot be explained with this model uncertainty. Generally, for larger h values, the A2S model predicts lower reflectivities than the IEM model, before both models asymptotically approach zero reflectivity for $h \gg 100$ mm. For the observation angles considered, $R^p_{\mathrm{A2S}}(h)$ monotonically

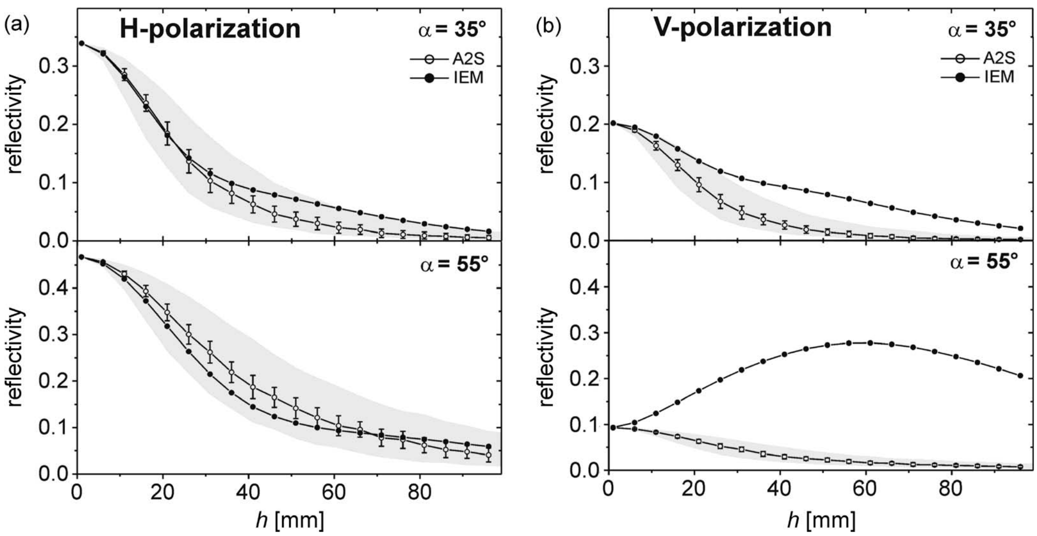

Fig. 6. (Open dots, ○) Rough surface reflectivities $R^p_{\mathrm{A2S}}(h)$ and (solid dots, ●) $R^p_{\mathrm{IEM}}(h)$ plotted versus h for $lc = 100$ mm, $\varepsilon_{\mathrm{s}} = 10$, and $\alpha = 35^\circ$ and 55°. Gray shaded areas are $R^p_{\mathrm{A2S}}(h)$ computed with different assumptions about the resolution limit Λ ranging from $\Lambda_{\mathrm{Bragg}}/2 \leq \Lambda \leq \Lambda_{\mathrm{Bragg}} \cdot 2$. The panels (a) are for horizontal polarization ($p = \mathrm{H}$), and the panels (b) are for vertical polarization ($p = \mathrm{V}$).

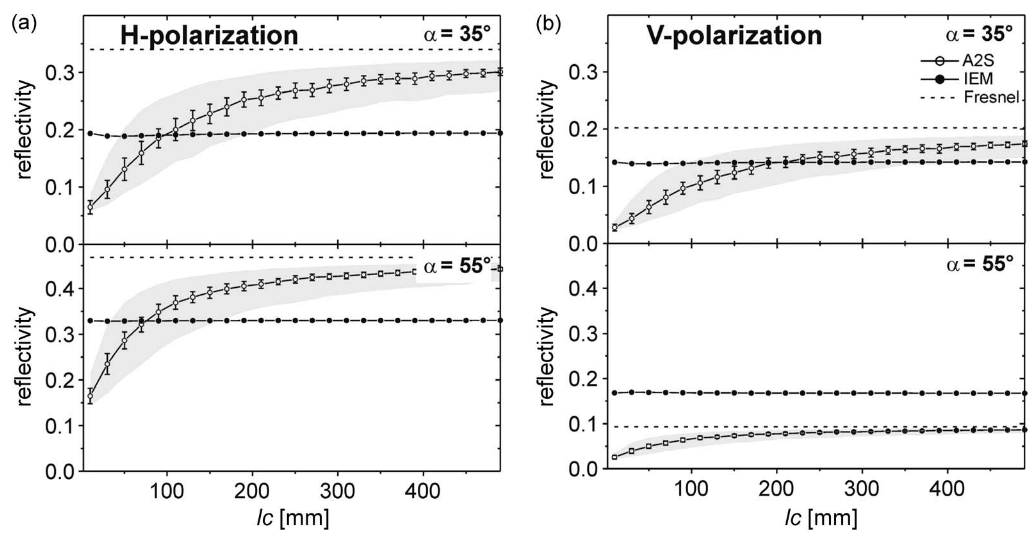

Fig. 7. (Open dots, ○) Rough surface reflectivities $R^p_{\mathrm{A2S}}(lc)$ and (solid dots, ●) $R^p_{\mathrm{IEM}}(lc)$ plotted versus lc for $h = 20$ mm, $\varepsilon_{\mathrm{s}} = 10$, and $\alpha = 35^\circ$ and 55°. Gray shaded areas are $R^p_{\mathrm{A2S}}(lc)$, computed with resolution limits Λ ranging from $\Lambda_{\mathrm{Bragg}}/2 \leq \Lambda \leq \Lambda_{\mathrm{Bragg}} \cdot 2$. The dashed lines are the corresponding F reflectivities R^p_{F}. The panels (a) are for horizontal polarization ($p = \mathrm{H}$), and the panels (b) are for vertical polarization ($p = \mathrm{V}$).

decreases with increasing h values, starting from values equal to R^p_{F}. The behavior of $R^p_{\mathrm{IEM}}(h)$ with respect to h, however, shows different regimes. Except for $p = \mathrm{V}$ and $\alpha = 55^\circ$, the reflectivities $R^p_{\mathrm{IEM}}(h)$ decrease in a manner similar to that of $R^p_{\mathrm{A2S}}(h)$ for small h values, but for intermediate h values, $R^p_{\mathrm{IEM}}(h)$ decreases much less distinctly or even increase. This is most pronounced for $\alpha = 55^\circ$ and vertical polarization, where $R^{\mathrm{V}}_{\mathrm{IEM}}(h)$ increases between $h = 0$ mm and $h = 60$ mm to values exceeding the corresponding F reflectivity $R^{\mathrm{V}}_{\mathrm{F}} \approx 0.1$.

These differing model responses with respect to h result in regimes where $R^p_{\mathrm{A2S}}(h)$ exceeds $R^p_{\mathrm{IEM}}(h)$ and vice versa. This observation can be explained as arising from polarization crosstalk effects, which changes a horizontally or a vertically polarized wave into an elliptically polarized wave. Such effects are accounted for in the IEM model but ignored in the A2S model. Polarization crosstalk is thought to be most pronounced with vertical polarization and with observation angles close to the Brewster angle $\alpha_{\mathrm{B}} = \mathrm{ArcTan}(\varepsilon_{\mathrm{s}}^{0.5}) \approx 72^\circ$ for $\varepsilon_{\mathrm{s}} = 10$. At these angles, $R^{\mathrm{H}}_{\mathrm{F}}$ are considerably higher than $R^{\mathrm{V}}_{\mathrm{F}}$, which can cause $R^{\mathrm{V}}_{\mathrm{IEM}}(h) > R^{\mathrm{V}}_{\mathrm{F}}$. However, as will be discussed in Section IV-C, this effect is rarely observed in the reflectivities $R^{\mathrm{V}}_{\mathrm{RM}}$ presented, which were derived from L-band brightness temperatures measured over bare soil. This indicates that the effect of polarization crosstalk might be overrated by the IEM model.

The results of the calculations for the model responses $R^p_{\mathrm{A2S}}(lc)$ and $R^p_{\mathrm{IEM}}(lc)$ on the correlation length lc are shown in Fig. 7 for $\alpha = 35^\circ$ and 55°. Distinct differences between $R^p_{\mathrm{A2S}}(lc)$ (open dots) and $R^p_{\mathrm{IEM}}(lc)$ (solid dots) can be observed in the figure as well.

$R^p_{\mathrm{A2S}}(lc)$ increase monotonically with increasing lc at H and V polarization. By contrast, $R^p_{\mathrm{IEM}}(lc)$ values are almost

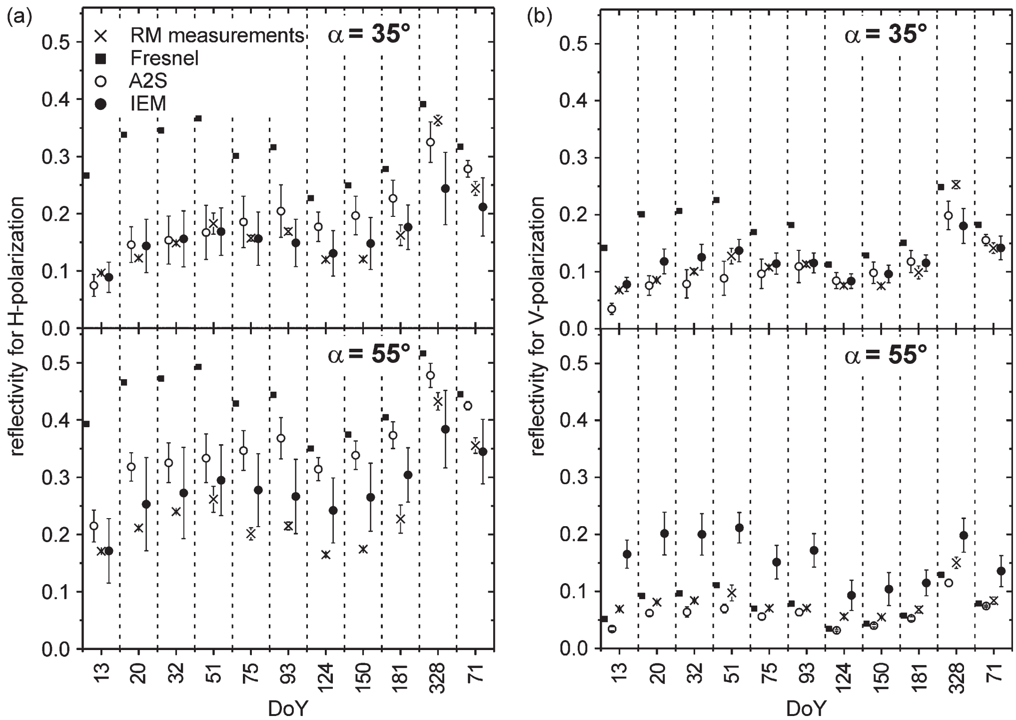

Fig. 8. Daily reflectivity ranges $\langle R_M^p \rangle \pm \sigma_M^p$ at $\alpha = 35^\circ$ and 55° for the 11 days indicated. ($\times$) Crosses represent the reflectivities derived from the RM measurements ($M = \mathrm{RM}$), ($\circ$) open dots are modeled with the A2S model ($M = \mathrm{A2S}$), ($\bullet$) solid dots are IEM predictions ($M = \mathrm{IEM}$), and (■) solid squares are the diurnal mean F reflectivities ($M = \mathrm{F}$). Panels (a) are for horizontal polarization ($p = \mathrm{H}$), and the panels (b) are for vertical polarization ($p = \mathrm{V}$).

constant within the parameter range investigated. This can be demonstrated by (1), showing that 1) the coherent part $R_{\mathrm{coh.}}^p$ of $R_{\mathrm{IEM}}^p(lc)$ is independent of lc and 2) the dependence of the noncoherent part $R_{\mathrm{non\text{-}coh}}^p$ is minor for $\alpha = 35^\circ$ and 55° and the exponential correlation function.

For lc values much larger than the wavelength $\lambda \approx 210$ mm, $R_{\mathrm{A2S}}^p(lc)$ values asymptotically approach values slightly smaller than the Fresnel reflectivities R_{F}^p (dashed lines). This is reasonable as their behavior approaches geometrical optics, which allows the footprint reflectivity to be represented as independent specular dielectric boundaries observed under a narrow range of locally varying observation angles (tangent-plane approximation). As the A2S model exclusively uses the SS roughness $[\Lambda = \Lambda_{\mathrm{Bragg}}$ (2)] to represent the dielectric transition zone $\varepsilon(z)$ (3), increasing $R_{\mathrm{A2S}}^p(lc)$ with increasing lc is inherently part of this model.

C. Comparison of Measured and Modeled Reflectivities

Using the data set presented in Section III, the IEM and the A2S models were tested against reflectivities derived from the L-band brightness temperatures T_{B}^p measured. The comparisons were made for the 11 days for which topography profiles, *in situ* soil permittivities ε_{s}, and temperatures T, as well as T_{B}^p are available.

For these days, the mean reflectivities $\langle R_{\mathrm{A2S}}^p \rangle$ and $\langle R_{\mathrm{IEM}}^p \rangle$ with corresponding standard deviations $\sigma_{R\ \mathrm{A2S}}^p$ and $\sigma_{R\ \mathrm{IEM}}^p$ were modeled on the basis of the 11–16 needle board profiles available per day. As can be seen from Figs. 3 and 5, the daily mean values of ε_{s}, h, and lc are well within the validity ranges of Shi's parameterization of IEM reflectivities (see Section II-A1). The ranges $\langle R_{\mathrm{A2S}}^p \rangle \pm \sigma_{R\ \mathrm{A2S}}^p$ and $\langle R_{\mathrm{IEM}}^p \rangle \pm \sigma_{R\ \mathrm{IEM}}^p$ were derived from the sets of daily reflectivities R_{A2S}^p and R_{IEM}^p, modeled following the procedures shown in Fig. 1. Since the type of correlation function was found to be persistently exponential for the entire observation period, only the exponential correlation function was considered when evaluating Shi's parameterization of the IEM model.

The ranges of measured reflectivities $\langle R_{\mathrm{RM}}^p \rangle \pm \sigma_{R\ \mathrm{RM}}^p$ were computed from 5 to 16 samples of R_{RM}^p, each deduced from the particular T_{B}^p measured. The sky brightness $T_{\mathrm{B,sky}} = 6.3$ K [34] was used in the radiative transfer model (4), and the soil temperature T used in (4) was derived from the mean values measured 1 and 5 cm below the soil surface. Although T_{B}^p are available for a wider range of α, the data presented are reduced to $\alpha = 35^\circ$ and 55° by averaging T_{B}^p over the adjacent observation angles (30°, 40° and 50°, 60°). This approach was chosen to simplify the visualization of the reflectivity data shown in Fig. 8. As the antenna field of view (13.5° at -3 dB) is of the same order of magnitude as the difference between the adjacent observation angles, no relevant information is lost by applying averaging. The reflectivities $\langle R_{\mathrm{A2S}}^p \rangle$, $\langle R_{\mathrm{IEM}}^p \rangle$, and $\langle R_{\mathrm{RM}}^p \rangle$, as well as the diurnal mean Fresnel reflectivities $\langle R_{\mathrm{F}}^p \rangle$ computed using the daily mean soil permittivities $\langle \varepsilon_{\mathrm{s}} \rangle$ from Fig. 3, are shown in Fig. 8.

The results show that $\langle R_{\mathrm{F}}^p \rangle$ values (solid squares) mostly significantly exceed the radiometrically derived $\langle R_{\mathrm{RM}}^p \rangle$ values (crosses). This indicates that it is surface roughness that mostly reduces the reflectivity. This experimental finding means that surface roughness should be considered when interpreting thermal L-band signatures, even though the rms surface height h is smaller than the Frauenhofer criterion [39]–[41]. It is only with vertical polarization that $\langle R_{\mathrm{RM}}^{\mathrm{V}} \rangle$ is found to be comparable with $\langle R_{\mathrm{F}}^{\mathrm{V}} \rangle$. For $\alpha = 35^\circ$, this is true solely for DoY 328, whereas

TABLE I

QUANTITIES δ_M AND OK_M USED FOR RATING THE MODEL PERFORMANCES AGAINST THE MEASUREMENTS $\langle R^p_{\rm RM}\rangle \pm \sigma^p_{R\ \rm RM}$ SHOWN IN FIG. 8. OK_M IS THE NUMBER OF DAYS, OUT OF THE TOTAL $n_{\rm DoY} = 11$ DAYS, ON WHICH EACH OF THE MODELS M = A2S, IEM, F CAN EXPLAIN THE MEASUREMENT. δ_M IS THE RELATIVE MODEL PREDICTION ERROR (12)

α [°]	p [-]	$OK_{\rm A2S}$ [-]	$\delta_{\rm A2S}$ [%]	$OK_{\rm IEM}$ [-]	$\delta_{\rm IEM}$ [%]	$OK_{\rm F}$ [-]	$\delta_{\rm F}$ [%]
35	H	7	24	10	12	0	97
35	V	9	20	9	16	1	68
55	H	0	51	7	23	0	92
55	V	2	26	0	102	3	16

for $\alpha = 55°$, the results show $\langle R^{\rm V}_{\rm F}\rangle \approx \langle R^{\rm V}_{\rm RM}\rangle$ for most days or even $\langle R^{\rm V}_{\rm RM}\rangle > \langle R^{\rm V}_{\rm F}\rangle$. The latter phenomenon is in accordance with the finding (see Section IV-B) that polarization crosstalk starts to dominate when the observation angle α approaches the Brewster angle $\alpha_{\rm B} = \mathrm{ArcTan}(\varepsilon_{\rm s}^{0.5})$.

Table I shows how δ_M and OK_M can be used to rate the performances of the A2S, IEM, and Fresnel models and compare them with the measurements $\langle R^p_{\rm RM}\rangle \pm \sigma^p_{R\ \rm RM}$ shown in Fig. 8.

The values OK_M indicate the number of days out of the total $n_{\rm DoY} = 11$ days for which the modeled ranges $\langle R^p_M\rangle \pm \sigma^p_{R\ M}$ (M = A2S, IEM, F) overlap with the measured $\langle R^p_{\rm RM}\rangle \pm \sigma^p_{R\ \rm RM}$. The mean relative deviations δ_M (in percent) given in Table I are computed as

$$\delta_M = \frac{100}{n_{\rm DoY}} \sum_{i=1}^{n_{\rm DoY}} \frac{\left|\langle R^p_M\rangle_i - \langle R^p_{\rm RM}\rangle_i\right|}{\langle R^p_{\rm RM}\rangle_i}. \qquad (12)$$

For $\alpha = 35°$ and horizontal polarization ($p = \rm H$), the A2S model explains the measurements $\langle R^{\rm V}_{\rm RM}\rangle \pm \sigma^{\rm V}_{R\ \rm RM}$ adequately on $OK_{\rm A2S} = 7$ of the $n_{\rm DoY} = 11$ days, the IEM model on $OK_{\rm IEM} = 10$ days, and the Fresnel model on $OK_{\rm F} = 0$, i.e., on no days. The corresponding mean relative errors are $\delta_{\rm A2S} = 24\%$, $\delta_{\rm IEM} = 12\%$, and $\delta_{\rm F} = 97\%$.

If $\alpha = 35°$ and polarization is vertical ($p = \rm V$), the measurements are explained at $OK_{\rm A2S} = OK_{\rm IEM} = 9$ days by both the A2S and the IEM models with $\delta_{\rm A2S} = 24\%$ and $\delta_{\rm IEM} = 12\%$. Again, the Fresnel model is inaccurate on most days except for DoY 328.

At the larger observation angle $\alpha = 55°$, the agreement between the measured daily reflectivities and the corresponding model predictions differ significantly depending on the polarization. If the polarization is horizontal, $\langle R^{\rm H}_{\rm A2S}\rangle$ systematically overshoots the measurements $\langle R^{\rm V}_{\rm RM}\rangle(OK_{\rm A2S} = 0$, $\delta_{\rm A2S} = 51\%)$, whereas $\langle R^{\rm H}_{\rm IEM}\rangle$ is consistent with the measurements $\langle R^{\rm V}_{\rm RM}\rangle$ on $OK_{\rm IEM} = 7$ days with $\delta_{\rm IEM} = 23\%$. Obviously, for $p = \rm H$ and $\alpha = 55°$, the IEM model performs better than the A2S model. However, with vertical polarization and $\alpha = 55°$, the reverse is true. In this case, $\langle R^{\rm V}_{\rm IEM}\rangle$ systematically overshoots the observations $\langle R^{\rm V}_{\rm RM}\rangle$, yielding $OK_{\rm IEM} = 0$ and $\delta_{\rm IEM} = 102\%$, whereas $\langle R^{\rm V}_{\rm A2S}\rangle$ reproduces the generally low $\langle R^{\rm V}_{\rm RM}\rangle$ clearly better ($OK_{\rm A2S} = 2$ and $\delta_{\rm A2S} = 26\%$). Although $\langle R^{\rm V}_{\rm A2S}\rangle$ and $\langle R^{\rm V}_{\rm RM}\rangle$ show close agreement for $\alpha = 55°$ and $p = \rm V$, the value $OK_{\rm A2S} = 2$ is low due to the corresponding small standard deviations $\sigma^{\rm V}_{R\ \rm A2S} \le 0.009$ and $\sigma^{\rm V}_{R\ \rm RM} \le 0.014$. It is interesting to note that $\sigma^p_{R\ \rm A2S}$ associated with the A2S predictions are significantly smaller for $\alpha = 55°$ than for $\alpha = 35°$. This can be explained by the way the L-band Bragg limit (2) decreases with increasing α (evaluating (2) for $\lambda = 21$ cm yields $\Lambda_{\rm Bragg} \approx 18$ cm for $\alpha = 35°$ and $\Lambda_{\rm Bragg} \approx 13$ cm for $\alpha = 55°$), which leads to increasingly restrictive spatial filtering for increasing α. The resolution limit $\Lambda = \Lambda_{\rm Bragg}$ used in the Fourier high-pass filter is not, however, an exact criterion (see Section IV-B), which implies that $OK_{\rm A2S}$ and $\sigma^{\rm V}_{R\ \rm A2S}$ for $\alpha = 55°$ and $p = \rm V$ could be optimized by changing the cutoff wavelength Λ.

The fact that the A2S model tends to overestimate the measured reflectivities with horizontal polarization and slightly underestimates them with vertical polarization can be explained by the presence or absence of polarization crosstalk. This effect is not accounted for in the A2S model, but it is incorporated in the IEM model. The systematic overestimates of the IEM reflectivities for $\alpha = 55°$ and $p = \rm V$, however, show that polarization crosstalk effects might be exaggerated in the IEM model. Polarization crosstalk is generally expected to gain importance when α approaches the Brewster angle, which is in the range $67° \le \alpha_{\rm B} \le 74°$, corresponding to the daily mean permittivities $5.7 \le \langle\varepsilon_{\rm s}\rangle \le 13$ of the measuring period. The A2S model was found to perform better than the IEM model for $p = \rm V$ and $\alpha = 55°$, which provides further support for this claim.

V. CONCLUSION

The impact of roughness on reflectivity has been analyzed by comparing the results of the A2S model [23], Shi's parameterization [27] of the IEM model [17], and the measurements in the field. The measurements were taken from the SMOSREX data set [37], consisting of L-band brightness temperatures $T^p_{\rm B}$ [38], *in situ* soil temperatures T and real parts of permittivities $\varepsilon_{\rm s}$, and mechanically measured topography profiles $f(x)$ on 11 days between January 2006 and February 2007.

The diurnal mean values of surface rms height $\langle h\rangle$, of correlation length $\langle lc\rangle$, and of $\langle EG\rangle$, expressing the ratio of surface features with spatial wavelengths smaller than lc, were investigated. During the 14-month experimental period after plowing the soil on DoY 13 in 2006, $\langle h\rangle$ was reduced from approximately 40 mm to almost half its value, while $\langle lc\rangle$ and $\langle EG\rangle$ remained at the same level over the experimental period. From this, it can be concluded that weathering reduces the coarse surface features distinctly, while the fine textures behave rather persistently. The finding that the measured $\langle EG\rangle$ values (11) were of the same order of magnitude as $EG_{\rm E}$ of an ideal exponential surface (7) has led us to conclude that the correlation function of a naturally weathered bare soil surface is exponential. Assuming that Shi's fast model is used in an operational data assimilation algorithm, this is important as Shi's parameterization requires specification of the type of surface autocorrelation function.

The responses of the two reflectivity models revealed distinct differences. Polarization crosstalk, which was not considered in the A2S model, was identified as one possible reason. Such effects could be considered in the A2S model by replacing the empirical effective medium approach (3) with a more realistic dielectric mixing model that takes anisotropies into account. Such a refinement would make it possible to consider not only the impact of topography on the reflectivity but also the impact of small scale dielectric anisotropies of the bulk soil within the A2S transition zone. This refinement would take into account the observation that, depending on the moisture level, such small scale dielectric heterogeneities can have a dominant impact on the reflectivity of bare soil [11], [23, Ch 4.7], [42]. It can then be assumed that the discrepancies between the measurements presented and the model predictions are associated with such volume effects occurring in the top few centimeters of the soil.

To sum up, the two roughness models performed reasonably in comparison with the measurements, although partly in complementary parameter ranges. The A2S model introduces some uncertainty by using a somewhat empirical spatial cutoff wavelength Λ to extract the small scale topography. Nevertheless, the performances of the A2S and the IEM model were very similar for $\alpha = 35^\circ$.

This paper has revealed that detailed knowledge of the soil topography might still not be sufficient for good predictions of the soil reflectivity as the dielectric heterogeneities and anisotropies of the bulk soil in the topmost centimeters can have more impact. To assess conclusively the implications of roughness model imperfections on the soil moisture retrieval from the upcoming SMOS and SMAP data, further model comparisons are required. These investigations should be conducted for different soil types and under different meteorological conditions, preferably utilizing corresponding satellite data.

Acknowledgment

The authors would like to thank the SMOSREX team members (N. E. D. Fritz, P. Waldteufel, R. Durbe, G. Cherel, J.-C. Poussière, M. J. Escorihuela, and C. Gruhier) for their valuable work on the fertile SMOSREX data set used in this work, J.-C. Calvet for coordinating the Météo-France Team, and S. Dingwall for the editorial work on the manuscript. M. Schwank would like to thank the "Deutsche Bahn AG" for permitting him to work on the manuscript undisturbed for many hours, commuting between work and his family.

References

[1] T. J. Jackson, D. M. LeVine, A. Y. Hsu, A. Oldak, P. J. Starks, C. T. Swift, J. D. Isham, and M. Haken, "Soil moisture mapping at regional scales using microwave radiometry: The Southern Great Plains hydrology experiment," *IEEE Trans. Geosci. Remote Sens.*, vol. 37, no. 5, pp. 2136–2151, Sep. 1999.

[2] E. G. Njoku, T. J. Jackson, V. Lakshmi, T. K. Chan, and S. V. Nghiem, "Soil moisture retrieval from AMSR-E," *IEEE Trans. Geosci. Remote Sens.*, vol. 41, no. 2, pp. 215–229, Feb. 2003.

[3] T. Schmugge, "Applications of passive microwave observations of surface soil moisture," *J. Hydrol.*, vol. 212/213, pp. 188–197, Dec. 1998.

[4] J.-P. Wigneron, Y. Kerr, P. Waldteufel, K. Saleh, M.-J. Escorihuela, P. Richaume, P. Ferrazzoli, P. de Rosnay, R. Gurney, J.-C. Calvet, J. P. Grant, M. Guglielmetti, B. Hornbuckle, C. Mätzler, T. Pellarin, and M. Schwank, "L-band Microwave Emission of the Biosphere (L-MEB) model: Description and calibration against experimental data sets over crop fields," *Remote Sens. Environ.*, vol. 107, no. 4, pp. 639–655, Apr. 2007.

[5] J. P. Grant, K. Saleh, A. A. Van de Griend, J.-P. Wigneron, M. Guglielmetti, Y. Kerr, M. Schwank, and N. Skou, "Calibration of the L-MEB model over a coniferous and a deciduous forest," *IEEE Trans. Geosci. Remote Sens.*, vol. 46, no. 3, pp. 808–818, Mar. 2008.

[6] T. Schmugge, "Remote sensing of soil moisture," in *Hydrological Forecasting*, M. G. Anderson and T. B. Burt, Eds. New York: Wiley, 1985, pp. 101–124.

[7] A. M. Shutko, "Microwave radiometry of lands under natural and artificial moistening," *IEEE Trans. Geosci. Remote Sens.*, vol. GRS-20, no. 1, pp. 18–26, Jan. 1982.

[8] *SMOS Earth Explorers*, 2000–2007. [Online]. Available: http://www.esa.int/esaLP/LPsmos.html

[9] Y. Kerr, P. Waldteufel, J.-P. Wigneron, J.-M. Martinuzzi, J. Font, and M. Berger, "Soil moisture retrieval from space: The Soil Moisture and Ocean Salinity (SMOS) mission," *IEEE Trans. Geosci. Remote Sens.*, vol. 39, no. 8, pp. 1729–1735, Aug. 2001.

[10] "The next decade of earth observations from space," *Earth Science and Applications from Space: National Imperatives for the Next Decade and Beyond*, 2007, Washington, DC: Nat. Acad. Press.

[11] M.-J. Escorihuela, Y. Kerr, P. de Rosnay, J.-P. Wigneron, J.-C. Calvet, and F. Lemaitre, "A simple model of the bare soil microwave emission at L-band," *IEEE Trans. Geosci. Remote Sens.*, vol. 45, no. 7, pp. 1978–1987, Jul. 2007.

[12] K. Schneeberger, M. Schwank, C. Stamm, P. de Rosnay, C. Mätzler, and H. Flühler, "Topsoil structure influencing soil water retrieval by microwave radiometry," *Vadose Zone J.*, vol. 3, no. 4, pp. 1169–1179, Nov. 2004.

[13] J.-P. Wigneron, L. Laguerre, and Y. Kerr, "A simple parameterization of the L-band microwave emission from rough agricultural soils," *IEEE Trans. Geosci. Remote Sens.*, vol. 39, no. 8, pp. 1697–1707, Aug. 2001.

[14] T. Mo and T. Schmugge, "A parameterization of the effect of surface roughness on microwave emission," *IEEE Trans. Geosci. Remote Sens.*, vol. GRS-25, no. 4, pp. 481–486, Jul. 1987.

[15] A. Monerris, A. Camps, and M. Vall-llossera, "Empirical determination of the soil emissivity at L-band: Effects of soil moisture, soil roughness, vine canopy, and topography," in *Proc. IEEE IGARSS*, Jul. 23–28, 2007, pp. 1110–1113.

[16] K. Saleh, J.-P. Wigneron, P. de Rosnay, M. J. Escorihuela, Y. Kerr, J.-C. Calvet, M. Schwank, and P. Waldteufel, "Estimates of surface soil moisture in prairies using L-band passive microwaves," in *Proc. IEEE IGARSS*, Jul. 23–28, 2007, pp. 1200–1203.

[17] A. K. Fung, *Microwave Scattering and Emission Models and Their Application*. Boston, MA: Artech House, 1994.

[18] L. Tsang, J. A. Kong, K.-H. Ding, and C. O. Ao, *Scattering of Electromagnetic Waves: Theories and Applications*, vol. I. New York: Wiley, 2000.

[19] L. Tsang, J. A. Kong, K.-H. Ding, and C. O. Ao, *Scattering of Electromagnetic Waves: Numerical Simulations*, vol. II. New York: Wiley, 2001.

[20] L. Tsang, J. A. Kong, K.-H. Ding, and C. O. Ao, *Scattering of Electromagnetic Waves: Advanced Topics*, vol. III. New York: Wiley, 2001.

[21] B. J. Choudhury, T. J. Schmugge, A. Chang, and R. W. Newton, "Effect of surface roughness on the microwave emission from soil," *J. Geophys. Res.*, vol. 84, no. C9, pp. 5699–5706, 1979.

[22] J. R. Wang and B. J. Choudhury, "Remote-sensing of soil-moisture content over bare field at 1.4 GHz frequency," *J. Geophys. Res.*, vol. 86, no. C6, pp. 5277–5282, 1981.

[23] C. Mätzler, P. W. Rosenkranz, A. Battaglia, and J. P. Wigneron, Eds., *Thermal Microwave Radiation—Applications for Remote Sensing*, ser. IET Electromagnetic Waves Series No. 52, vol. 52. London, U.K.: IET, 2006.

[24] J. P. Grant, A. A. Van de Griend, M. Schwank, and J.-P. Wigneron, "Observations and modeling of a pine forest floor at L-band," *IEEE Trans. Geosci. Remote Sens.*, vol. 47, no. 7, pp. 2024–2034, Jul. 2009.

[25] M. Schwank, M. Guglielmetti, C. Mätzler, and H. Flühler, "Testing a new model for the L-band radiation of moist leaf litter," *IEEE Trans. Geosci. Remote Sens.*, vol. 46, no. 7, pp. 1982–1994, Jul. 2008.

[26] M. Schwank, C. Mätzler, M. Guglielmetti, and H. Flühler, "L-band radiometer measurements of soil water under growing clover grass," *IEEE Trans. Geosci. Remote Sens.*, vol. 43, no. 10, pp. 2225–2237, Oct. 2005.

[27] J. Shi, K. S. Chen, Q. Li, T. Jackson, P. E. O'Neill, and L. Tsang, "A parameterized surface reflectivity model and estimation of bare-surface soil moisture with L-band radiometer," *IEEE Trans. Geosci. Remote Sens.*, vol. 40, no. 12, pp. 2674–2686, Dec. 2002.

[28] T. D. Wu, K. S. Chen, J. Shi, and A. K. Fung, "A transition model for the reflection coefficient in surface scattering," *IEEE Trans. Geosci. Remote Sens.*, vol. 39, no. 9, pp. 2040–2050, Sep. 2001.

[29] G. C. Topp, J. L. Davis, and A. P. Annan, "Electromagnetic determination of soil water content: Measurements in coaxial transmission lines," *Water Resour. Res.*, vol. 16, no. 3, pp. 574–582, 1980.

[30] A. Sihvola, *Electromagnetic Mixing Formulas and Applications*, ser. Electromagnetic Waves Series 47. London, U.K.: IEE, 1999.

[31] J. R. Birchak, C. G. Gardner, J. E. Hipp, and J. M. Victor, "High dielectric constant microwave probes for sensing soil moisture," *Proc. IEEE*, vol. 62, no. 1, pp. 93–98, Jan. 1974.

[32] M. Bass, E. W. Van Stryland, D. R. Williams, and W. L. Wolfe, Eds., "Optical properties of films and coatings, part 11," in *Handbook of Optics*. New York: McGraw-Hill, 1995, pp. 42.9–42.14.

[33] A. Chanzy, Y. Kerr, J.-P. Wigneron, and J.-C. Calvet, "Soil moisture estimation under sparse vegetation using microwave radiometry at C-band," in *Proc. IEEE IGARSS*, 1997, vol. 3, pp. 1090–1092.

[34] T. Pellarin, J.-P. Wigneron, J. C. Calvet, M. Berger, H. Douville, P. Ferrazzoli, Y. H. Kerr, E. Lopez-Baeza, J. Pulliainen, L. P. Simmonds, and P. Waldteufel, "Two-year global simulation of L-band brightness temperatures over land," *IEEE Trans. Geosci. Remote Sens.*, vol. 41, no. 9, pp. 2135–2139, Sep. 2003.

[35] L. Tsang, J. A. Kong, K.-H. Ding, and C. O. Ao, *Scattering of Electromagnetic Waves: Numerical Simulations*. New York: Wiley, 2001.

[36] M. Nishimoto, "Error analysis of soil roughness parameters estimated from measured surface profile data," in *Proc. IEEE IGARSS*, Boston, MA, 2008, pp. II-719–II-722.

[37] P. de Rosnay, J.-C. Calvet, Y. Kerr, J.-P. Wigneron, F. Lemaître, M.-J. Escorihuela, J. Muñoz Sabater, K. Saleh, J. Barrié, G. Bouhours, L. Coret, G. Cherel, G. Dedieu, R. Durbe, F. N. E. Dine, F. Froissard, J. Hoedjes, A. Kruszewski, F. Lavenu, D. Suquia, and P. Waldteufel, "SMOSREX: A long term field campaign experiment for soil moisture and land surface processes remote sensing," *Remote Sens. Environ.*, vol. 102, no. 3/4, pp. 377–389, Jun. 2006.

[38] F. Lemaître, J. C. Poussière, Y. H. Kerr, M. Déjus, R. Durbe, P. de Rosnay, and J. C. Calvet, "Design and test of the ground-based L-band radiometer for estimating water in soils (LEWIS)," *IEEE Trans. Geosci. Remote Sens.*, vol. 42, no. 8, pp. 1666–1676, Aug. 2004.

[39] F. T. Ulaby, R. Moore, and A. K. Fung, *Microwave Remote Sensing, Active and Passive, vol I, Microwave Remote Sensing Fundamentals and Radiometry*. Norwood, MA: Artech House, 1981.

[40] F. T. Ulaby, R. Moore, and A. K. Fung, *Microwave Remote Sensing, Active and Passive, vol II, Radar Remote Sensing and Surface Scattering and Emission Theory*. Norwood, MA: Artech House, 1982.

[41] F. T. Ulaby, R. Moore, and A. K. Fung, *Microwave Remote Sensing, Active and Passive, vol III, From Theory to Applications*. Norwood, MA: Artech House, 1986.

[42] E. Schanda, "On randomly absorbing and scattering surface layers," *IEEE Trans. Geosci. Remote Sens.*, vol. GRS-20, no. 1, pp. 72–76, Jan. 1982.

Mike Schwank received the Ph.D. degree in physics from the Swiss Federal Institute of Technology (ETH), Zürich, Switzerland, in 1999. The topic of his Ph.D. thesis was "nanolithography using a high-pressure scanning-tunneling microscope."

In the following three years, he gained experience in the industrial environment, where he was a Research and Development Engineer in the field of micro-optics. Since 2003, he has been working in the research field of microwave remote sensing applied to soil moisture detection. Currently, he is a Senior Research Assistant with the Swiss Federal Institute for Forest, Snow and Landscape Research (WSL), Birmensdorf, Switzerland. His research involves practical and theoretical aspects of microwave radiometry. In addition to his research at the WSL, he is also with the company Gamma Remote Sensing Research and Consulting AG, Gümligen, Switzerland, where he is involved in the production of microwave radiometers to be deployed for ground-based Soil Moisture and Ocean Salinity calibration/validation purposes.

Ingo Völksch received the B.S. degree in geology from the University of Jena, Jena, Germany, and the M.S. degree in earth sciences with a special focus on glaciology from the Swiss Federal Institute of Technology (ETH) Zürich, Zürich, Switzerland, in 2004, with his thesis entitled "Monitoring and modeling of small-scale spatial variations of mountain permafrost properties." In the following year, he gained further experience in permafrost modeling and snow hydrology, working as a Research Assistant with the Swiss Federal Institute of Snow and Avalanche Research (SLF), Davos, Switzerland.

He then turned his focus toward passive microwave radiometry and is currently working toward the Ph.D. degree in the mountain hydrology group of the Swiss Federal Institute for Forest, Snow and Landscape Research (WSL), Birmensdorf, Switzerland.

His work focuses on L-band signatures of soils with oriented surface structures.

Jean-Pierre Wigneron (SM'03) received the B.S. degree in engineering from SupAéro, Ecole Nationale Supérieure de l'Aéronautique et de l'Espace, Toulouse, France, in 1987 and the Ph.D. degree from the University of Toulouse, Toulouse, in 1993.

He is currently a Senior Research Scientist with the Institut National de Recherche Agronomiques, Bordeaux, France, where he is the Head of the remote sensing team in the Ecologie Fonctionnelle et Physique de l'Environnement (EPHYSE). He coordinated the development of the L-band Microwave Emission of the Biosphere model for soil and vegetation in the Level-2 inversion algorithm of the European Space Agency Soil Moisture and Ocean Salinity Mission. He has been a member of the Editorial Board of *Remote Sensing of Environment* since 2005. His research interests are in microwave remote sensing of soil and vegetation, radiative transfer, and data assimilation.

Yann H. Kerr (M'88–SM'01) received the B.S. degree in engineering from the Ecole Nationale Supérieure de l'Aéronautique et de l'Espace, Toulouse, France, the M.Sc. degree in electronics and electrical engineering from Glasgow University, Glasgow, U.K., and the Ph.D. degree from the Université Paul Sabatier, Toulouse.

From 1980 to 1985, he was with Centre National d'Etudes Spatiales. In 1985, he joined Laboratoire d'Etudes et de Recherches en Télédétection Spatiale, for which he was Director in 1993–1994. He spent 19 months with the Jet Propulsion Laboratory, Pasadena, CA, in 1987–1988. He has been with the Centre d'Etudes Spatiales de la Biosphère, Centre National de la Recherche Scientifique/Centre National d'Etudes Spatiales/Institut de Recherche pour le Développement/Universite Paul Sabatier, Toulouse, France, since 1995 (Deputy Director and Director since 2007). His fields of interest are in the theory and techniques for microwave and thermal infrared remote sensing of the Earth, with emphasis on hydrology, water resource management, and vegetation monitoring. He has been involved with many space missions. He was an Earth Observing Satellite Principal Investigator (PI) (interdisciplinary investigations) and a PI and Precursor of the use of the SCAT over land. In 1990, he started to work on the interferometric concept applied to passive microwave Earth observation and was subsequently the Science Lead on the Microwave Imaging Radiometer with Aperture Synthesis (MIRAS) project for the European Space Agency (ESA) with Matra Marconi Space and Observatoire Midi-Pyrénées. He was also a Coinvestigator on IRIS, OSIRIS, and HYDROS for the National Aeronautics and Space Administration. He was the Science Advisor for the Multifrequency Imaging Microwave Radiometer and a Coinvestigator on the Advanced Microwave Scanning Radiometer. In 1997, he first proposed the natural outcome of the previous MIRAS work with what was to become the Soil Moisture and Ocean Salinity (SMOS) Mission which was eventually selected by ESA in 1999 with him as the SMOS Mission Lead Investigator and Chair of the Science Advisory Group. He is also in charge of the SMOS science activity coordination in France. He has organized all the SMOS Science workshops.

Arnaud Mialon received the M.S. degree in climate and physics–chemistry of the atmosphere from the Université Joseph Fourier de Grenoble, Grenoble, France, in 2002 and the Ph.D. degrees in ocean–atmosphere–hydrology from the Université Joseph Fourier de Grenoble and in remote sensing from the Université de Sherbrooke, Sherbrooke, QC, Canada, in 2005.

He joined the Centre d'Etudes Spatiales de la Biosphère, Centre National de la Recherche Scientifique/Centre National d'Etudes Spatiales/ Institut de Recherche pour le Développement/Universite Paul Sabatier, Toulouse, France, in 2006. His fields of interest are focused on passive microwave remote sensing of continental surfaces. He is involved in the Soil Moisture and Ocean Salinity mission as well as the Surface Monitoring of the Soil Reservoir Experiment field experiment.

Patricia de Rosnay received the Ph.D. degree from the University Pierre et Marie Curie, Paris, France, in 1999.

She is currently a Research Scientist with the European Centre for Medium-Range Weather Forecasts, Reading, U.K., where she works on land surface data assimilation for numerical weather prediction applications. Her current research interests are focused on the use of passive and active microwave data for soil moisture analysis in weather forecast models. She is involved in the Soil Moisture and Ocean Salinity (SMOS) Validation and Retrieval Team and participates in the European Organisation for the Exploitation of Meteorological Satellites Satellite Application Facility on Support to Operational Hydrology and Water Management (EUMETSAT H-SAF) project. She has been also involved in land surface modeling activities such as the African Monsoon Multidisciplinary Analysis Land Surface Model Intercomparison Project (ALMIP) and the microwave component of the project ALMIP-Microwave Emission Model. She initiated the validation of the future SMOS soil moisture products over West Africa. She has been working for four years with the Centre d'Etudes Spatiales de la Biosphère, Centre National de la Recherche Scientifique/Centre National d'Etudes Spatiales/Institut de Recherche pour le Développement/Universite Paul Sabatier, Toulouse, France, where she has been having an active contribution to the Surface Monitoring of the Soil Reservoir Experiment field experiment for soil moisture remote sensing with the SMOS project. Her research topic at the Laboratoire de Météorologie Dynamique from 1994 to 2001 was focused on global scale land surface process understanding and parameterization developments for climate modeling.

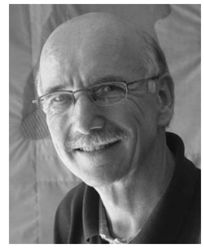

Christian Mätzler (M'96–SM'03) studied physics at the University of Bern with minors in mathematics and geography, M.Sc. degree in 1970, and Ph.D. degree in solar radio astronomy in 1974.

After postdoctoral research with the NASA Goddard Space Flight Center, Greenbelt, MD, and with the Swiss Federal Institute of Technology (ETH) Zürich, Zürich, Switzerland, he returned to the Institute of Applied Physics, University of Bern, in 1978 as a Research Group Leader for terrestrial and atmospheric radiometry and remote sensing. He received the habilitation in applied physics with emphasis on remote sensing methods in 1986 and the title of a Titular Professor in the same field in 1992. He spent sabbaticals in 1996 at the Universities of Colorado and Washington and in 2004 at the Paris Observatory. His studies have been concentrated on microwave (1–100 GHz) signatures for active and passive remote sensing of the atmosphere, snow, ice, soil, and vegetation, as well as the development of methods for dielectric and propagation measurements for such media, while complementary work has been done in his group at infrared and optical wavelengths. He is the Editor of a book on thermal microwave emission with applications for remote sensing. He is interested in the understanding of the observed processes and in the interactions between surface and atmosphere. Based on the experimental work, he has contributed to the development of radiative transfer models, on methods for retrieving geophysical parameters from microwave remote sensors, and on the assessment of optimum sensor parameters.